Supporting Information

Chemical Framework to Design Linear-like Relaxors toward Capacitive Energy Storage

Hui Liu[1,*,#], Zheng Sun[1,#], Ji Zhang[2,#], Huajie Luo[1], Yuanpeng Zhang[3], Andrea Sanson[4], Manuel Hinterstein[5], Laijun Liu[6], Joerg C. Neuefeind[3], and Jun Chen[1,7,*]

[1]Beijing Advanced Innovation Center for Materials Genome Engineering, Department of Physical Chemistry, University of Science and Technology Beijing, Beijing 100083, China

[2]School of Materials Science and Engineering, Nanjing University of Science and Technology, Nanjing, Jiangsu 210094, China

[3]Chemical and Engineering Materials Division, Oak Ridge National Laboratory, Oak Ridge, Tennessee 37831, USA

[4]Department of Physics and Astronomy & Department of Management and Engineering, University of Padova, Padova I-35131, Italy

[5]Fraunhofer IWM, Institute for Materials Mechanics, 79108 Freiburg, Germany

[6]College of Materials Science and Engineering, Guilin University of Technology, Guilin 541004, China

[7]Hainan University, Haikou 570228, Hainan Province, China

[#]Hui Liu, Zheng Sun, and Ji Zhang contribute equally to this work.

*Corresponding author. huiliu@ustb.edu.cn and junchen@ustb.edu.cn

Method:

Sample preparation: $(Bi_{0.35}K_{0.175}Ba_{0.3}Na_{0.175})(Ti_{0.7}Zr_{0.3})O_3$ (BKT-D1), and $(Ba_{0.45}Bi_{0.35}Ca_{0.2})(Ti_{0.65}Sc_{0.35})O_3$ (BT-D2) solid solution ceramics were prepared by the solid-state reaction method. The dried raw powder including Bi_2O_3 (99.9%, 3% excess), Na_2CO_3 (99.8%, 3% excess), K_2CO_3 (99%, 5% excess), $BaCO_3$ (99.95%), TiO_2 (98%), ZrO_2 (99.99%), Sc_2O_3 (99%) and Nb_2O_5 (99.9%) were weighed according to the stoichiometric ratio. The mixture was then planetary ball-milled with ethanol for 12 h. After drying, the mixed powders were calcined at 800 ~ 850 °C for 2 h. Some of the calcined powders were pressed into pellets and sintered at 1080 ~ 1180 °C for 1~3 h, with the remaining powders used to compensate for the evaporation loss of K, Na, and Bi in a closed crucible. The surface layers of the sintered pellets were removed, and some of the pellets were ground into powders for further analysis.

Phase and crystal structure identification: The room temperature high-energy synchrotron X-ray powder diffraction was performed at the P02.1 beamline of the PETRA III facility by using an X-ray wavelength of 0.2074 Å with a Varex XRD 4343CT 2D detector at a distance from the sample of 2200 mm[1].

Microstructural characterizations: The surface morphologies of ceramics were analyzed using a field-emission scanning electron microscopy (LEO1530, ZEISS SUPRA 55, Oberkochen, Germany). High-resolution bright-field TEM images, grain morphology, and corresponding selected area electron diffraction were conducted on an image-aberration corrected scanning transmission electron microscopy (Titan ETEM G2, Thermo Fisher Scientific, USA) operated at 300 kV. Atomic-scale high-angle dark-field annular (HAADF) STEM images were recorded using a scanning transmission microscopy (JEM-F200, JEOL, Japan) equipped with probe and image aberration-correctors operated at 200 kV. To remove noise, all HAADF-STEM images were Fourier-filtered using a lattice mask. The position and intensity of

atomic columns were determined by fitting with a two-dimensional Gaussian function, and the angle and magnitude of atomic displacements were calculated using a MATLAB script.

Electrical properties measurements: The ferroelectric tester (model aixACCT, TF Analyzer 1000) was used to test the low electric-field bipolar *P-E* loops on ceramic disks with a diameter of 10 mm and a thickness of 0.5 mm. The tests were conducted at room temperature and a frequency of 1 Hz. The dielectric spectra were measured using a dielectric spectrum measurement system (LDM-500, China), while the electrochemical impedance was measured using a Precision impedance analyzer (Agilent 4294A, USA).

Capacitive energy storage properties measurements:

For dielectric capacitors, the total energy storage density (W), energy storage density (W_{rec}) and energy storage efficiency (η) are given by:

$$W = \int_0^{P_{max}} EdP$$

$$W_{rec} = \int_{P_r}^{P_{max}} EdP$$

$$\eta = \frac{W_{rec}}{W}$$

Where, E is the applied field and P_{max} and P_r are the maximum and remanent polarization, respectively.

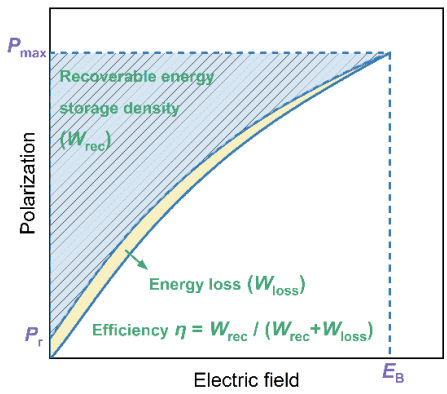

Diagrammatic illustration of dielectric energy storage. The shaded area indicates the energy storage density W_{rec}.

The energy storage properties were measured on bulk ceramic samples with thickness of 50-70 μm, and gold electrodes with an area of approximately 0.8 mm^2. The bulk ceramic samples were polished under water to thicknesses of about 50-70 μm using lapping films (3M) coated with successively finer aluminium oxide particles. The final polish was done using a slurry of 0.05-μm colloidal silica in an alkaline suspension. A gold electrode was evaporated onto one face of the bulk ceramics, serving as the bottom electrode. Gold point-electrodes with an approximate area of about 0.8 mm^2 (about 1.0 mm in diameter) were deposited on the top side of the pellets to serve as the top electrode. The ferroelectric tester from Radiant Technologies Inc., USA was used to test the unipolar *P-E* loops at various electric fields, frequencies, and temperatures in silicone oil. The discharge characteristics, with an overdamped value of 51 Ω, were measured using Tongguo (TG) technology (CFD-003, China). To assess cyclic stability, the samples were subjected to a cyclic electric field at 10 kHz. After cycling, the energy-storage properties were determined by measuring the unipolar *P-E* loops of the fatigued samples under 40 kV mm^{-1} for BKT-D1 and 50 kV mm^{-1} for BT-D2 at 10 Hz.

Total scattering measurements: The neutron total scattering data were collected at room temperature using the Nanoscale-Ordered Materials Diffractometer (NOMAD) at the Spallation Neutron Source (SNS), Oak Ridge National Laboratory. The powder sample was loaded in quartz capillaries. The data, which had a Q_{max} of 35 $Å^{-1}$, were processed using the ADDIE software to correct for attenuation, inelasticity effects, multiple scattering, and background. The pair distribution function $G(r)$ was then determined by Fourier transforming the corrected total scattering structure function $S(Q)$. To assess the instrument resolution, total scattering data for NIST Si SRM powder were also measured. The calculated total-scattering data were adjusted for the instrument resolution in both reciprocal and real spaces. It should be noted that the

distinct neutron scattering lengths of various elements (Table S5) allowed for the differentiation of element-specific structural information.

Big-box refinement based on the Reverse Monte Carlo method: The Bragg Rietveld refinement was performed with GSAS-II software using the neutron Bragg data to obtain the long-range average crystal structure parameters (Table S1). Reverse Monte Carlo (RMC) fitting was performed on the RMCprofile software[2,3]. The obtained long-range average cubic structure was expanded to a 20×20×20 super-cell (about 80×80×80 $Å^3$) with containing 40000 atoms (including 2800 Bi atoms, 1400 K atoms, 1400 Na atoms, 2400 Ba atoms, 5600 Ti atoms, 2400 Zr atoms, and 24000 O atoms). The *A*/*B*-site atoms were randomly distributed initially. In the RMC simulations, the neutron *G(r)*, *S(Q)*, and Bragg data, in total three data, were simultaneously fitted under bond valence sum constraints and coordination constraints. *A*-site and *B*-site atoms were allowed to swap. During the RMC simulation process, RMCprofile automatically optimizes the weights among the fitting data. Each RMC modeling was run to generate more than 10^3 moves per atom to get converged. The details of the analysis of the polar atomic displacements and unit-cell polar vectors from the refined 3D atom configurations can be found in our previous works[4-56]. To get the statistical analysis results, 20 refined 3D atom configurations were merged together.

EXAFS. Room temperature Bi L_{III}-edge EXAFS spectra were collected in transmission mode at the XAFS beamline of ELETTRA Sincrotrone Trieste during the experiment no. 20230135. The sample for EXAFS was prepared by mixing and pelletizing the sample powder with boron nitride powder. The amount of sample powder was chosen to have an absorption edge jump $\Delta\mu x \sim 1$. The EXAFS signal was extracted by using Athena and Artemis software[7,8], and FEFF8[9] was employed to calculate the Bi-O (and Bi-(Ti)) scattering amplitudes and phases shift, using $BiTiO_3$ as reference. An in-house software based on FEFFIT code was developed to perform the best-fitting simulation of the EXAFS Fourier transform (FT) between ~0.5 and 3.5 Å. The preliminary simulations demonstrate that two distinct Bi-O distributions (+

one longer Bi-(Ti) distance distribution) are needed to fit the FT structure (Fig. S16). Various best-fitting simulations with different FT intervals and k-weight were performed, and then averaged (Fig. S17).

Calculation of electronic charge density based on the density functional theory. The electronic charge density from the respective clusters in a refined 3D atomic configuration based on the density functional theory calculations (Fig. 4j and Fig. S19). The first-principles calculations are based on density functional theory within the Perdew-Burke-Ernzerhof approximation[10], as implemented in the Vienna ab initio simulation package[11]. Interactions between ion cores and valence electrons are described by the projector augmented wave method[12]. Plane waves with a kinetic energy cutoff of 500 eV are used as the basis set.

Mechanical performance measurements. The Vickers hardness values of sample were tested by wolpert wilson instruments (401MVD, China). The applied load for each indentation process was set at 9.8 N with a dwell time of 15 s.

Supplementary Figures and Tables

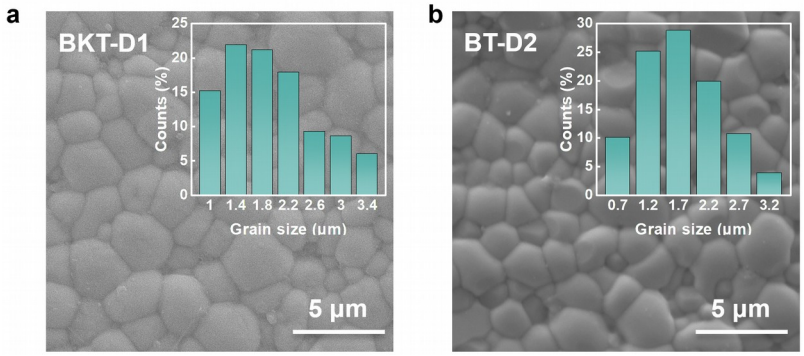

Figure S1. SEM images of BKT-D1 and BT-D2 ceramics, the insets indicate the corresponding statistical distribution of grain size.

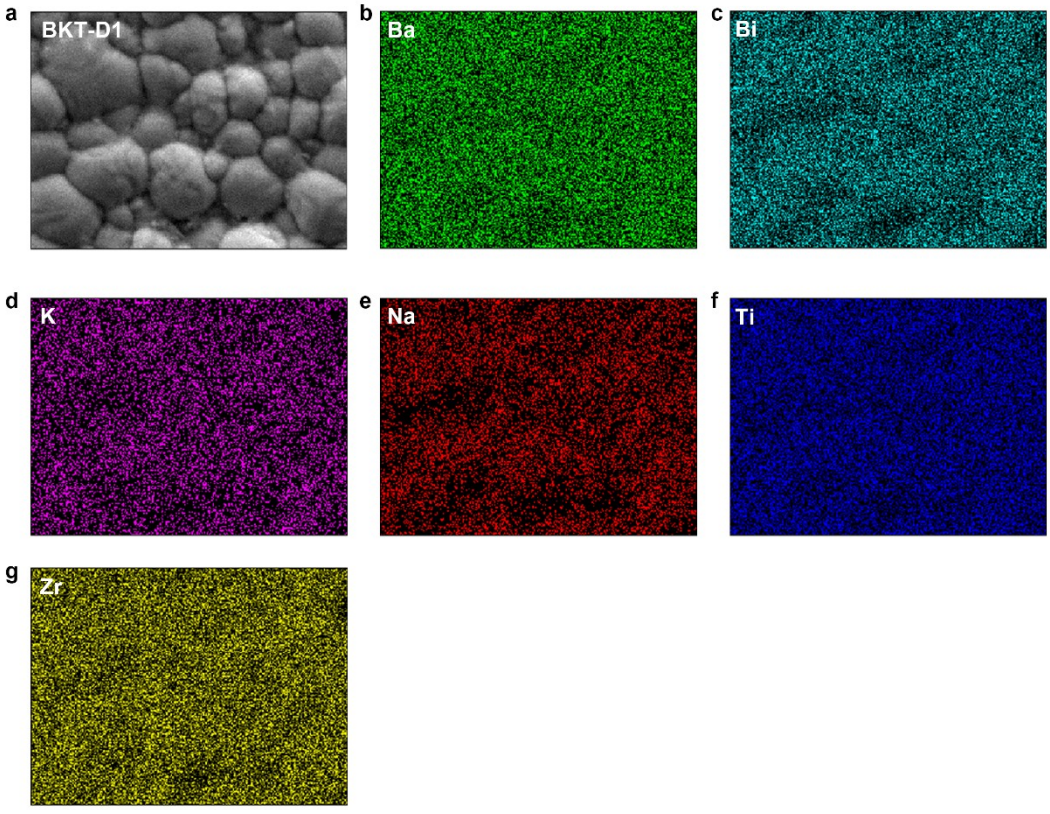

Figure S2. (a) SEM surface morphology and (b-g) the corresponding element mapping of BKT-D1.

Table S1. Crystal structure parameters of BKT-D1 obtained from Rietveld refinement.

BKT-D1					
Space group: *Pm* -3*m*					
Cell parameters: $a = b = c = 4.0256$ Å, $\alpha = \beta = \gamma = 90°$					
atom type	occupancy	atomic coordinate			Uiso
		x	*y*	*z*	
Bi	0.35	0	0	0	0.070
Na	0.175	0	0	0	0.070
K	0.175	0	0	0	0.070
Ba	0.3	0	0	0	0.070
Ti	0.7	0.5	0.5	0.5	0.009
Zr	0.3	0.5	0.5	0.5	0.009
O	1	0.5	0	0.5	0.020
*R*w = 6.5%, GOF = 2.0					

Table S2. Crystal structure parameters of BT-D2 obtained from Rietveld refinement.

BT-D2					
Space group: *Pm* -3*m*					
Cell parameters: $a = b = c = 4.0213$ Å, $\alpha = \beta = \gamma = 90°$					
atom type	occupancy	atomic coordinate			Uiso
		x	*y*	*z*	
Ba	0.45	0	0	0	0.050
Ca	0.2	0	0	0	0.050
Bi	0.35	0	0	0	0.050
Ti	0.65	0.5	0.5	0.5	0.005
Sc	0.35	0.5	0.5	0.5	0.005
O	1	0.5	0	0.5	0.022
*R*w = 7.6%, GOF = 2.7					

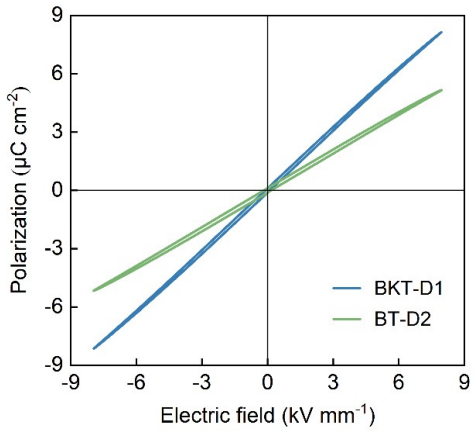

Figure S3. Bipolar *P*-*E* loops of BKT-D1, and BT-D2 ceramics measured at the lower electric field of 8 kV mm^{-1} at 1 Hz at room temperature.

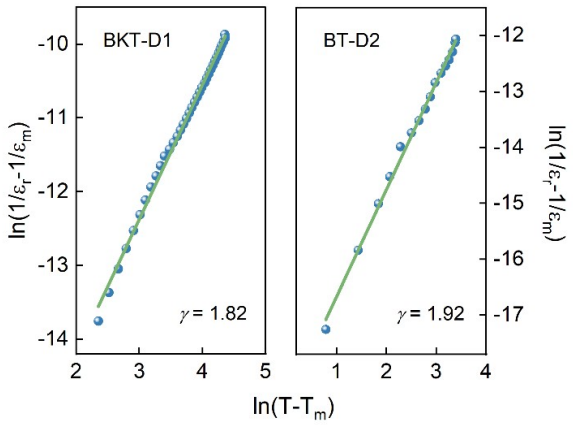

Figure S4. Characterization of the diffuseness parameter γ based on the modified Curie-Weiss distribution.

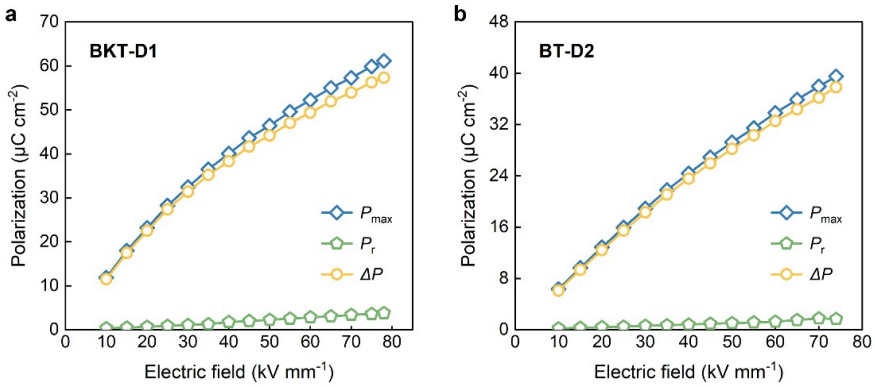

Figure S5. The extracted P_r, P_m, and ΔP as function of the electric field. (a) BKT-D1 and (b) BT-D2.

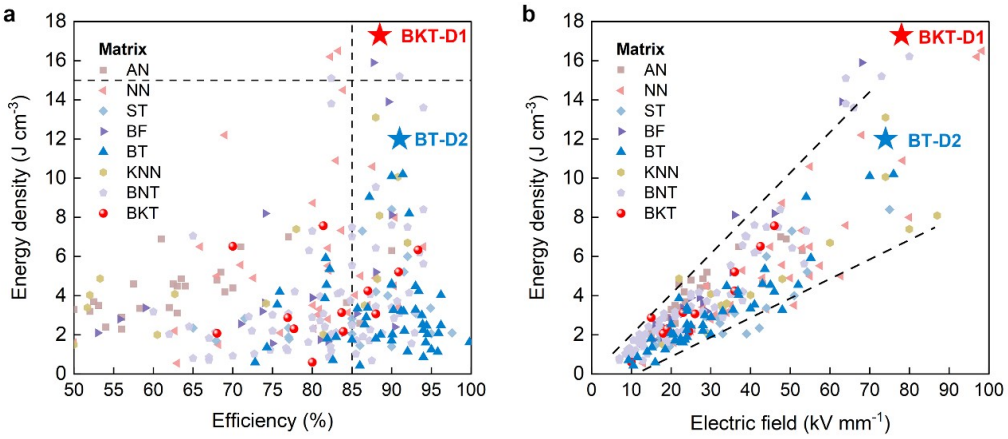

Figure S6. Comparison of W_{rec} versus (a) efficiency (η), (b) E_b between BKT-D1 and

BT-D2 bulk ceramics, and other reported lead-free bulk ceramics.

Table S3. A comparison of W_{rec} and η between BKT-D1 and other reported BKT-based lead-free bulk ceramics.

Composition	W_{rec} (J cm^{-3})	η (%)	Reference
0.5BKT–0.5ST	0.6	80	Ref.[13]
BKT-0.06LMT	2.08	68	Ref. [14]
SBKT-2*wt.*% Er_2O_3	2.17	83.9	Ref.[15]
0.7BKT-0.3ST	2.31	77.7	Ref.[16]
0.76 BKT-0.24BF	2.88	76.9	Ref. [17]
0.95(0.5BKT–0.5ST)–0.05BZT	3.07	88	Ref. [18]
BKT-0.15BMN	3.14	83.7	Ref.[19]
0.96(0.6BKT-0.4SBT)-0.04BMH	4.25	87	Ref.[20]
0.6 (0.75BKT-0.25BF)-0.4SBT	5.21	90.87	Ref.[21]
0.5(0.7BKT-0.25BF)-0.5CT	6.34	93.32	Ref.[22]
0.84(0.6BKT-0.4BF)-0.16NSN	6.52	70	Ref.[23]
0.6BKT-0.3BT-0.1NN	7.57	81.4	Ref. [24]
BKT-D1	**17.3**	**88.5**	**This work**

Table S4. A comparison of W_{rec} and η between BT-D2 and other reported BT-based lead-free bulk ceramics.

Composition	W_{rec} (J cm^{-3})	η (%)	Reference
BTMN	0.43	86	Ref. [25]
BCZT	0.59	72.8	Ref. [26]
0.91BT-0.09BY	0.71	82.6	Ref. [27]
0.9BT-0.1BY-MWS	0.86	94	Ref. [28]
0.9BT-0.1BMN	1.13	95.8	Ref. [29]
BSZT	1.15	92	Ref. [30]
0.85BT-0.15BMZ	1.25	95	Ref. [31]
0.92(0.65BT-0.35BNT)-0.08SYN	1.36	74.3	Ref. [32]
0.8BT-0.15BMZ	1.61	94.3	Ref. [33]

0.88BST-0.12BZN	1.62	99.8	Ref. [34]
Mn-doped 0.9BT-0.1BMN	1.7	90	Ref. [35]
BSCT	1.75	85	Ref. [36]
0.88BT-0.12BMT	1.81	88	Ref. [37]
CuO doped BSCTZ	1.81	81.9	Ref. [38]
0.875BT-0.125BMN	1.89	83	Ref. [39]
BSTM–2 *wt.*% MgO	2.01	88.6	Ref. [40]
0.9BBNT-0.1SSN	2.02	90.1	Ref. [41]
0.96BT-0.04KN	2.03	94.5	Ref. [42]
0.88BT-0.12BNN	2.09	95.9	Ref. [43]
0.85BT–0.15BZS	2.21	91.6	Ref. [44]
0.88BT-0.12BMS	2.25	94	Ref. [45]
0.92BT-0.08BZZ	2.47	94.4	Ref. [46]
0.84BT-0.16BNZ	2.49	96.2	Ref. [47]
0.85BCT-0.15NNT	2.53	86.6	Ref. [48]
0.9BT-0.1BNS	2.53	93.9	Ref. [49]
0.85BT-0.15BMZ	2.9	86.8	Ref. [50]
0.88BT-0.12BLZ	3	93.8	Ref. [51]
Gd-doped 0.7BT-0.3SBT	3.2	91.5	Ref. [52]
0.6BZT-0.4BNT	3.22	91.2	Ref. [53]
0.92BT-0.08LZH	3.27	90.22	Ref. [54]
0.88BT-0.12BMT	3.28	93	Ref. [55]
0.9BST-0.1BMN	3.34	85.7	Ref. [56]
0.9BT-0.1BMH	3.38	87	Ref. [57]
0.65BLT-0.35SBT	3.54	75.6	Ref. [58]
0.95BT-0.05BMT-Sm	3.86	81.6	Ref. [59]
0.65BT-0.35(SBT-BMZ)	4.03	96.2	Ref. [60]
BSBNT	4.2	75.9	Ref. [61]
0.9[0.9BCT-0.1BLZ]–0.1BNT	4.23	93.4	Ref. [62]
0.6BT-0.4BMT	4.49	93	Ref. [63]
0.93BST-0.07BMN	4.55	81.8	Ref. [64]
BT-0.06BMN	4.55	90	Ref. [65]
0.4BS-0.55BT-0.05NN	4.6	90	Ref. [66]
0.3BCZT-0.7ST-0.3mol% MnO_2	5.36	82.2	Ref. [67]
0.93BSZT-0.07BMN	5.92	81.7	Ref. [68]
BNBSCT-2mol% PbO	8.2	92.2	Ref. [69]
0.85(0.8BT-0.2BNT)-0.15CZ	9.04	87.2	Ref. [70]
BBT	10.1	90	Ref. [71]
0.8(0.97BT-0.3NN)-0.2BZZ	10.2	91.4	Ref. [72]
BT-D2	**12**	**91**	**This work**

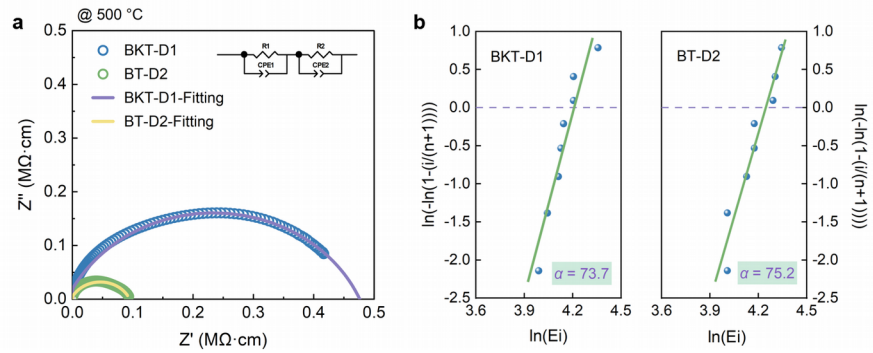

Figure S7. (a) The impedance fitting spectrum at 500 °C of BKT-D1 and BT-D2. The inset shows the calculated band gap. (c) Fitting the Weibull distribution of BKT-D1 and BT-D2.

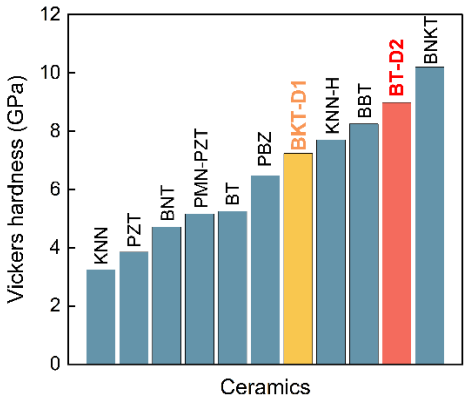

Figure S8. A comparison of Vickers hardness (H_v) between the designed BKT-D1, BT-D2 and some representative perovskite ceramics.

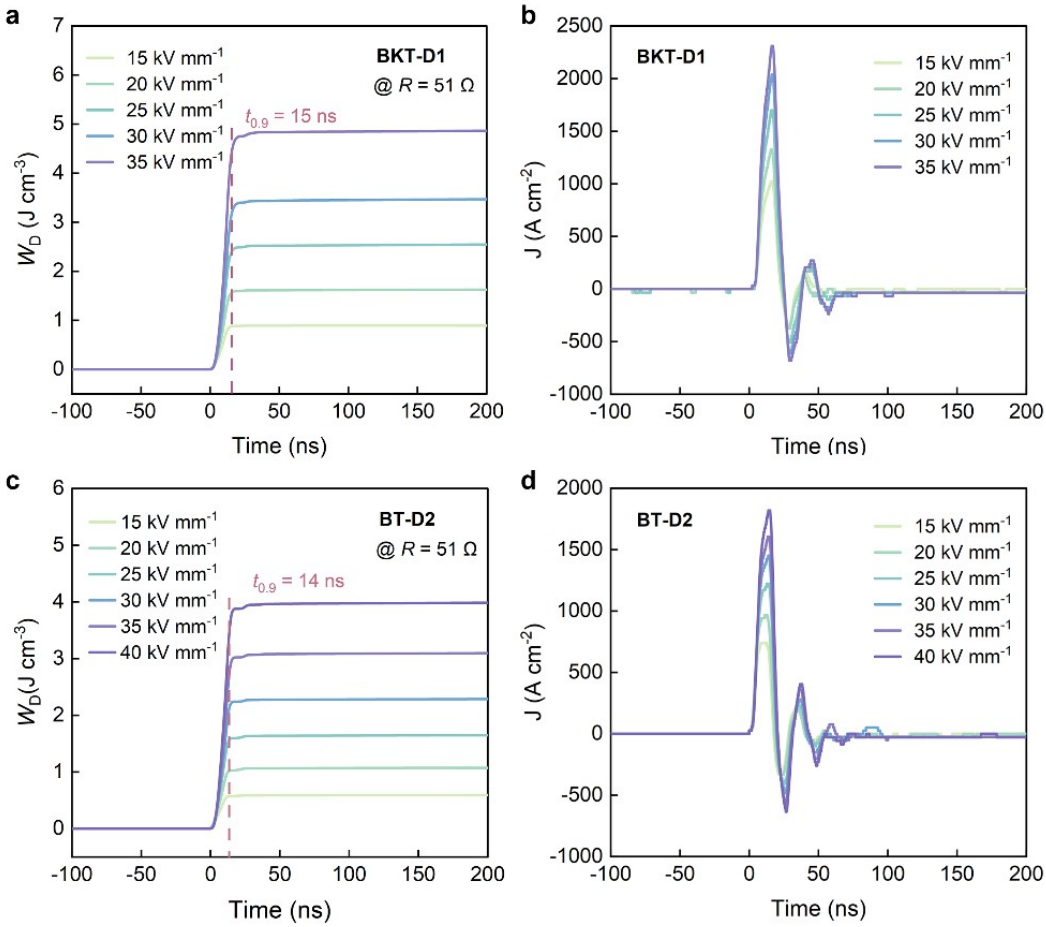

Figure S9. Charge-discharge performance of BKT-D1 and BT-D2. (a) and (c) overdamped discharge energy density. (b) and (d) underdamped discharge waveforms. Note that the applied maximum electric field values during the charge-discharge performance tests are relatively lower compared to those applied for the unipolar polarization curve tests. This is due to the breakdown of the electrodes, rather than the breakdown of the dielectric ceramics themselves in charge-discharge performance tests. If the electrodes of the charge-discharge instrument are optimized, higher electric field values can be applied.

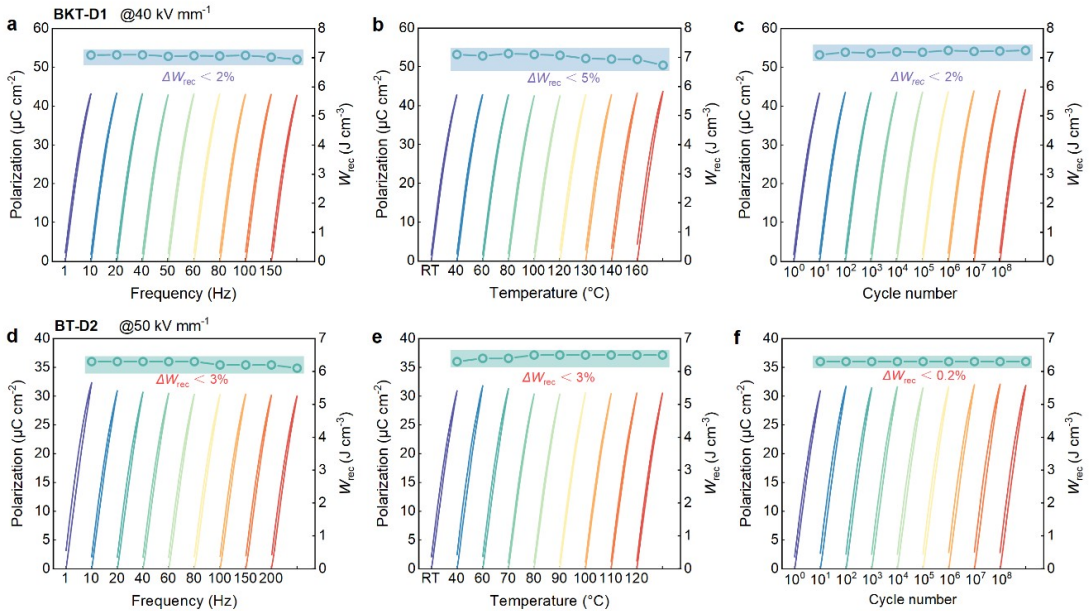

Figure S10. Unipolar *P-E* loops and the W_{rec} obtained from reliability testing measured at 40 kV mm^{-1} for BKT-D1 and 50 kV mm^{-1} for BT-D2.

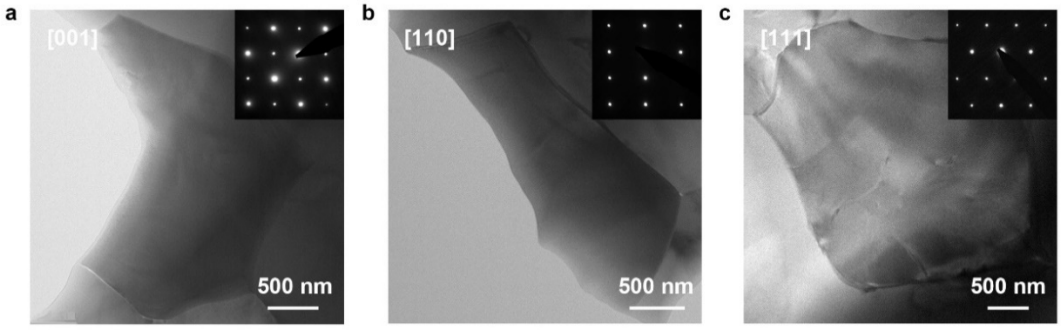

Figure S11. Grain morphology and corresponding SAED captured by high-resolution bright-field TEM images along (a) $[001]_c$, (b) $[110]_c$, (c) $[111]_c$.

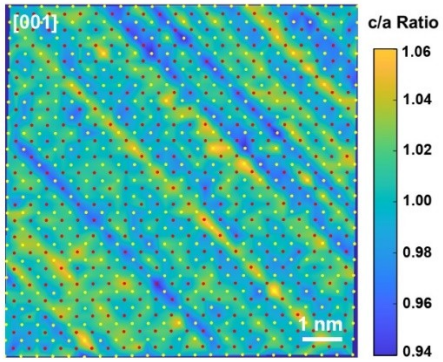

Figure S12. The corresponding lattice distortion (*c*/*a*) mapping of Fig. 3b.

Table S5. The neutron scattering lengths of the elements contained in BKT-D1.

Elemen t	Neutron scattering lengths (fm)
Bi	8.532
Na	3.63
Ba	5.07
K	3.67
Ti	-3.438
Zr	7.16
O	5.803

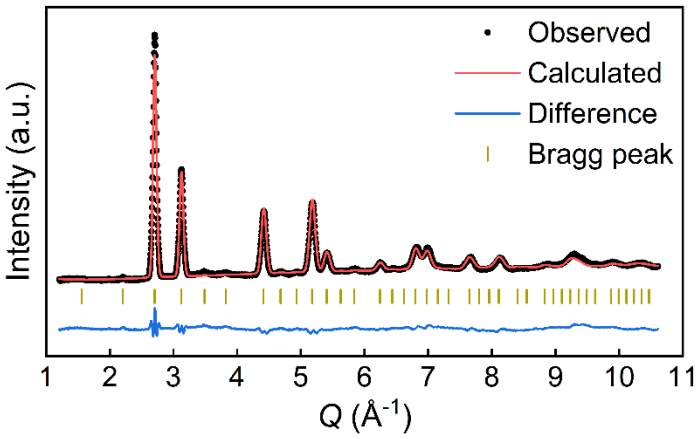

Figure S13. The RMC fitting of neutron Bragg data for BKT-D1.

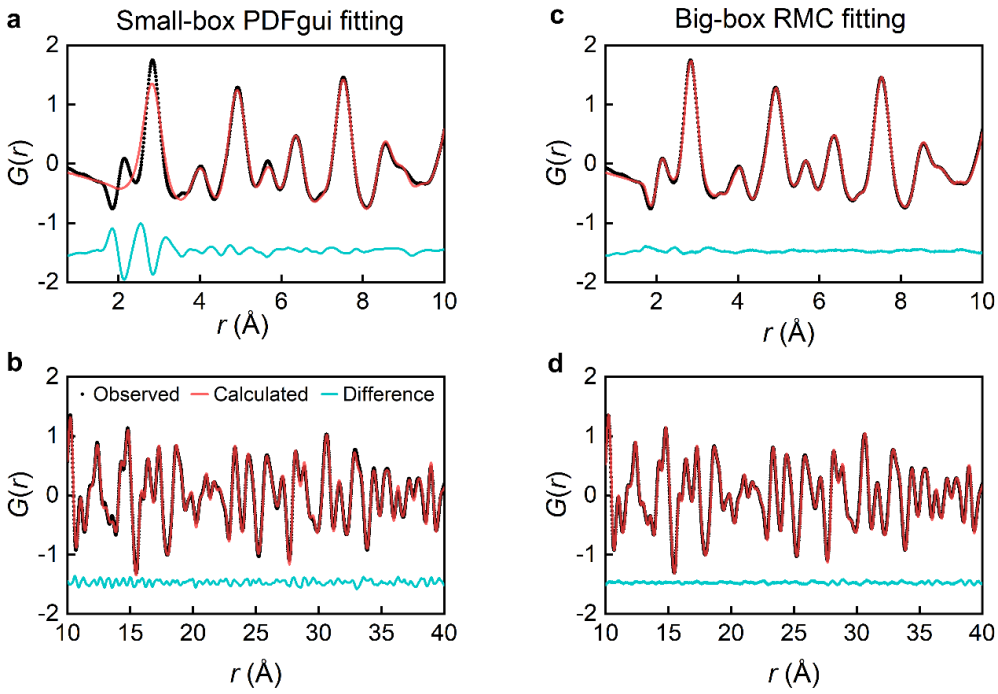

Figure S14. Comparison of the fitting results of neutron PDF of BKT-D1 between the small-box method by using a cubic model (a,b) and the big-box RMC method (c,d).

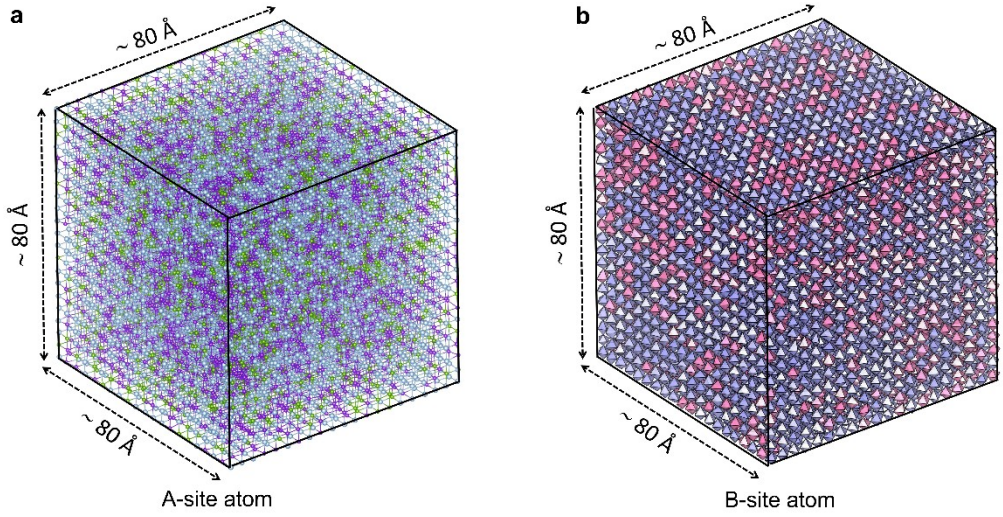

Figure S15. Atomic distribution of BKT-D1 in a refined 3D atom configuration. (a) *A*-site atomic distribution. The purple, green, and wathet atoms indicate the Bi, Na, K/Ba, respectively. (b) BO_6 distribution. The pink and lila indicate the TiO_6, and ZrO_6, respectively.

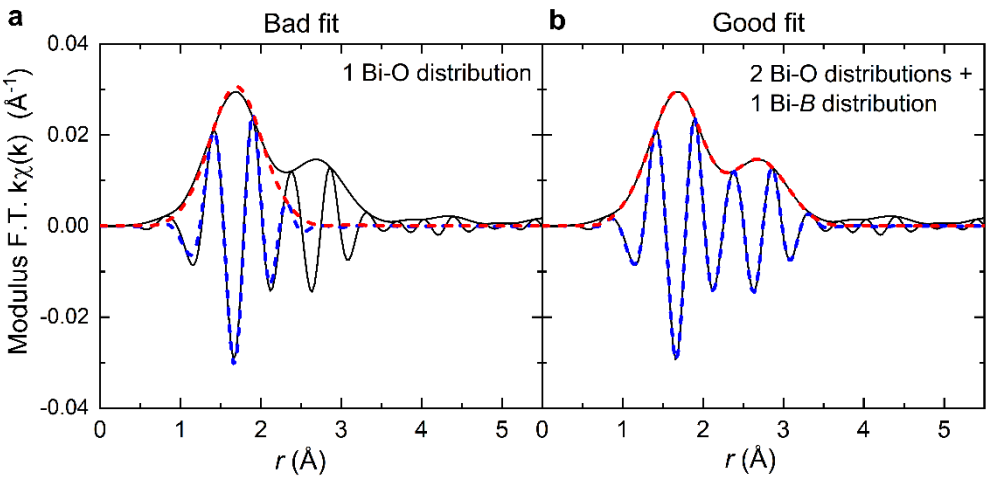

Figure S16. Example of best fitting-simulation of the Bi-L_{III} EXAFS FT (here *k*=2-14 Å-1, *k*, Gauss) between *R*=0.5-3.5 Å by using: (a) one Bi-O distance distribution and (b) two Bi-O + one longer Bi-(Ti) distance distributions. It can be observed as all three distributions must be included to fit the FT structure.

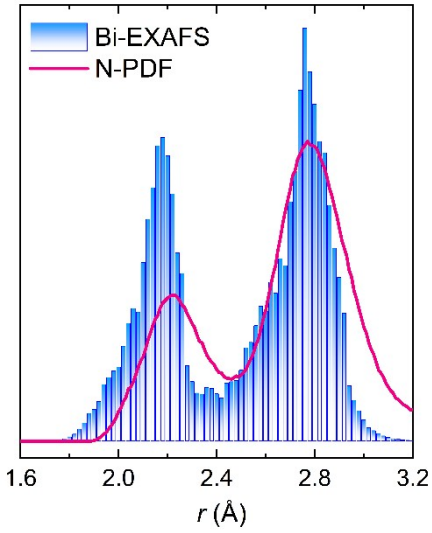

Figure S17. Bi-O distance distribution obtained by Bi L_{III} EXAFS best-fitting simulation and its comparison with partial Bi-O PDFs obtained from neutron total scattering.

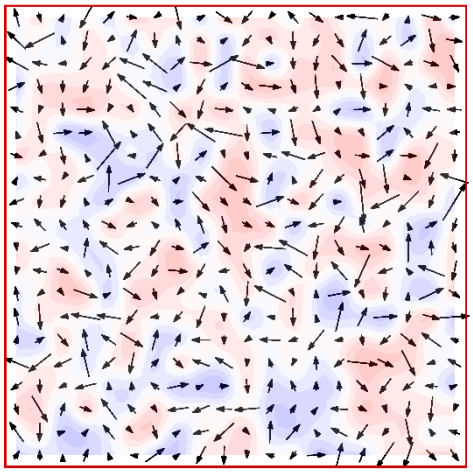

Figure S18. 2D displacement distribution obtained from one of the refined 3D atomic configurations viewed along $[001]_c$. The vector indicates the vector of the *B*-site position atom relative to the center of its four nearest neighboring *A*-site positions, which is an average of 10 unit cells (with thickness about 4 nm) along the $[001]_c$ direction.

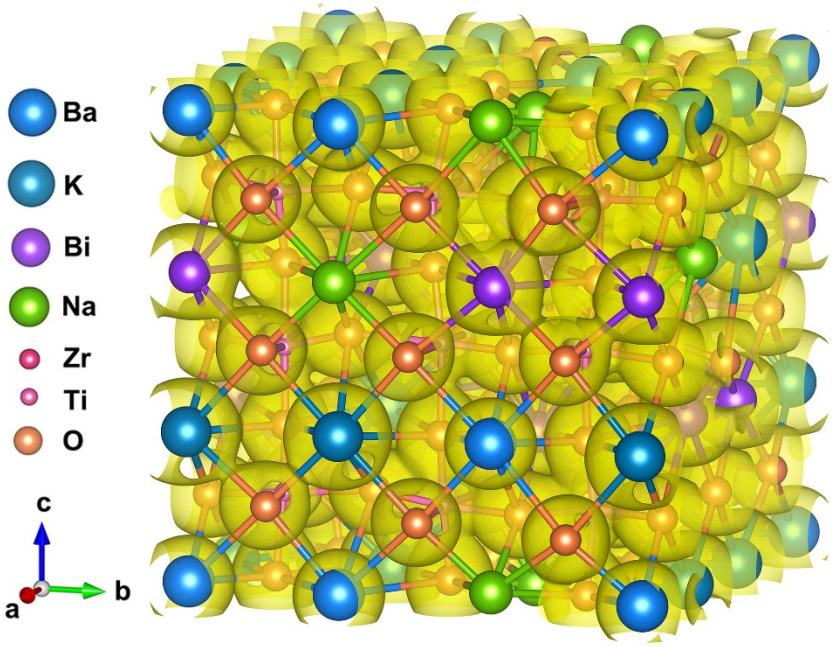

Figure S19. The calculated electronic charge density from the respective clusters in a refined 3D atomic configuration based on the density functional theory calculations, showing the valence electron localization isosurfaces visualized for a value of 0.2 e Å^{-3}.

Supplementary References

1() Herklotz, M.; Scheiba, F.; Hinterstein, M.; Nikolowski, K.; Knapp, M.; Dippel, A.-C.; Giebeler, L.; Eckert, J.; Ehrenberg, H. Advances in in situ powder diffraction of battery materials: a case study of the new beamline P02.1 at DESY, Hamburg. *J. Appl. Crystallogr.* **2013**, *46*, 1117.

2() Tucker, M. G.; Keen, D. A.; Dove, M. T.; Goodwin, A. L.; Hui, Q. RMCProfile: Reverse Monte Carlo for Polycrystalline Materials. *J. Phys.: Condens. Matter* **2007**, *19*, 335218.

3() Krayzman, V.; Levin, I.; Woicik, J. C.; Proffen, Th.; Vanderah, T. A.; Tucker, M. G. A Combined Fit of Total Scattering and Extended X-Ray Absorption Fine Structure Data for Local-Structure Determination in Crystalline Materials. *J. Appl. Cryst.* **2009**, *42*, 867-877.

4() Liu, H.; Sun, Z.; Sun, S.; Zhang, Y.; Luo, H.; Qi, H.; Liu, L.; Neuefeind, J. C.; Xing, X.; Chen, J. Evolving differentiated local polar displacement and relaxor behavior in $Pb(Mg_{1/3}Nb_{2/3})O_3$−$PbTiO_3$ perovskites. *Chem. Mater.* **2022**, *34*, 3985−3992.

5() Sun, Z.; Zhang, J.; Luo, H.; Yao, Y.; Wang, N.; Chen, L.; Li, T.; Hu, C.; Qi, H.; Deng, S.; Gallington, L. C.; Zhang, Y.; Neuefeind, J. C.; Liu, H.; Chen, J. Superior Capacitive Energy-Storage Performance in Pb-Free Relaxors with a Simple Chemical Composition. *J. Am. Chem. Soc.* **2023**, *145*, 6194–6202.

6() Liu, H.; Shi, X.; Yao, Y; Luo, H.; Li, Q.; Huang, H.; Qi, H.; Zhang, Y.; Ren, Y.; Kelly, S. D.; Roleder, K.; Neuefeind, J. C.; Chen, L.-Q.; Xing, X.; Chen, J. Emergence of High Piezoelectricity from Competing Local Polar Order-Disorder in Relaxor Ferroelectrics. *Nat Commun.* **2023**, *14*, 1007.

7() Ravel, B. & Newville, M. ATHENA, ARTEMIS, HEPAESTUS: data analysis for X-ray absorption spectroscopy using IFEFFIT. *J. Synch. Rad.* 12, 537–541 (2005).

8() Swartz, S. L. & Shrout, T. R. Fabrication of perovskite lead magnesium niobate. *Mat. Res. Bull.* **17**, 1245–1250 (1982).

9() A. L. Ankudinov, B. Ravel, J. J. Rehr, S. D. Conradson, Real-space multiplescattering calculation and interpretation of X-ray absorption near-edge structure. *Phys. Rev. B* **58**, 7565–7576 (1998).

10() Perdew, J. P.; Burke, K.; Ernzerhof, M. *Phys. Rev. Lett.* **1996**, *77*, 3865-3868.

11() Kresse, G.; Furthmüller, *J. Comp. Mater. Sci*. **1996**, *6*, 15-50.

12() Blöchl, P. E. *Phys. Rev. B* **1994**, *50*, 17953-17979.

13() Shiga, M.; Hagiwara, M.; Fujihara, S. $(Bi_{1/2}K_{1/2})TiO_3$–$SrTiO_3$ Solid-Solution Ceramics for High-Temperature Capacitor Applications. *Ceram. Int.* **2020**, *46*, 10242–10249.

14() Li, F.; Jiang, T.; Zhai, J.; Shen, B.; Zeng, H. Exploring Novel Bismuth-Based Materials for Energy Storage Applications. *J. Mater. Chem. C* **2018**, *6*, 7976-7981.

15() Zhao, P.; Tang, B.; Fang, Z.; Si, F.; Yang, C.; Zhang, S. Improved Dielectric Breakdown Strength and Energy Storage Properties in Er_2O_3 modified $Sr_{0.35}Bi_{0.35}K_{0.25}TiO_3$. *Chem. Eng. J* **2021**, *403*, 126290.

16() Li, F.; Si, R.; Li, T.; Wang, C.; Zhai, J. High Energy Storage Performance and Fast Discharging Speed in Dense $0.7Bi_{0.5}K_{0.5}TiO_3$-$0.3SrTiO_3$ Ceramics via a Novel Rolling Technology. *Ceram. Int.* **2020**, *46*, 6995–6998.

17() Yang, Q.; Zhu, M.; Wei, Q.; Zhang, M.; Zheng, M.; Hou, Y. Excellent Energy Storage Performance of $K_{0.5}Bi_{0.5}TiO_3$-Based Ferroelectric Ceramics under Low Electric Field. *Chem. Eng. J* **2021**, *414*, 128769.

18() Wei, Y.; Zhang, N.; Jin, C.; Shen, J.; Xie, J.; Dai, Z.; Hu, L.; Zeng, Y.; Jian, Z. A $Bi_{1/2}K_{1/2}TiO_3$-Based Ergodic Relaxor Ceramic for Temperature-Stable Energy Storage Applications. *Mater. Des.* **2021**, *207*, 109887.

19() Li, F.; Hou, X.; Li, T.; Si, R.; Wang, C.; Zhai, J. Fine-Grain Induced Outstanding Energy Storage Performance in Novel $Bi_{0.5}K_{0.5}TiO_3$–$Ba(Mg_{1/3}Nb_{2/3})O_3$ Ceramics via a Hot-Pressing Strategy. *J. Mater. Chem. C* **2019**, *7*, 12127-12138.

20() Kang, R.; Wang, Z.; Zhao, Y.; Li, Y.; Hu, Y.; Hao, X.; Zhang, L.; Lou, X. Enhanced Energy Storage

Performance of $Bi_{0.5}K_{0.5}TiO_3$-Based Ceramics via Composition Modulation. *J. Alloys Compd.* **2023**, *935*, 167999.

21() Niu, Z.; Zheng, P.; Xiao, Y.; Luo, C.; Zhang, K.; Zhang, J.; Zheng, L.; Zhang, Y.; Bai, W. $Bi_{0.5}K_{0.5}TiO_3$-Based Lead-Free Relaxor Ferroelectric with High Energy Storage Performances via the Grain Size and Bandgap Engineering. *Mater. Today Chem.* **2022**, *24*, 100898.

22() Zheng, L.; Niu, Z.; Zheng, P.; Zhang, K.; Luo, C.; Zhang, J.; Wang, N.; Bai, W.; Zhang, Y. Simultaneously Achieving High Energy Storage Performance and Remarkable Thermal Stability in $Bi_{0.5}K_{0.5}TiO_3$-Based Ceramics. *Mater. Today Energy* **2022**, *28*, 101078.

23() Wang, H.; Li, E.; Wei, K.; Li, H.; Xing, M.; Zhong, C. Significantly Enhanced Energy Storage Performance in High Hardness BKT-Based Ceramic via Defect Engineering and Relaxor Tuning. *ACS Appl. Mater. Interfaces* **2022**, *14*, 54021–54033.

24() Chen, L.; Long, F.; Qi, H.; Liu, H.; Deng, S.; Chen, J. Outstanding Energy Storage Performance in High-Hardness $(Bi_{0.5}K_{0.5})TiO_3$-Based Lead-Free Relaxors via Multi-Scale Synergistic Design. *Adv. Funct. Mater.* **2022**, *32*, 2110478.

25() Liu, W.; Gao, J.; Zhao, Y.; Li, S. Significant Enhancement of Energy Storage Properties of $BaTiO_3$-Based Ceramics by Hybrid-Doping. *J. Alloys Compd.* **2020**, *843*, 155938.

26() Zhan, D.; Xu, Q.; Huang, D.-P.; Liu, H.-X.; Chen, W.; Zhang, F. Dielectric Nonlinearity and Electric Breakdown Behaviors of $Ba_{0.95}Ca_{0.05}Zr_{0.3}Ti_{0.7}O_3$ Ceramics for Energy Storage Utilizations. *J. Alloys Compd.* **2016**, *682*, 594-600.

27() Shen, Z.; Wang, X.; Luo, B.; Li, L. $BaTiO_3$–$BiYbO_3$ Perovskite Materials for Energy Storage Applications. *J. Mater. Chem. A* **2015**, *3*, 18146-18153.

28() Yi, X.; Ji, C.; Chen, J.; Yang, H.; Yong, H.; Fu, C.; Cai, W.; Gao, R.; Fan, T.; Wang, Z.; Deng, X. Effects of Sintering Method and $BiAlO_3$ Dopant on Dielectric Relaxation and Energy Storage Properties of $BaTiO_3$–$BiYbO_3$ Ceramics. *Phys. Status Solidi A* **2020**, *217*, 1900721.

29() Wang, T.; Jin, L.; Li, C.; Hu, Q.; Wei, X. Relaxor Ferroelectric $BaTiO_3$–$Bi(Mg_{2/3}Nb_{1/3})O_3$ Ceramics for EnergyStorage Application. *J. Am. Ceram. Soc.* **2015**, *98*, 559–566.

30() Sun, Z.; Li, L.; Yu, S.; Kang, X.; Chen, S. Energy Storage Properties and Relaxor Behavior of Lead-Free $Ba_{1-x}Sm_{2x/3}Zr_{0.15}Ti_{0.85}O_3$ Ceramics. *Dalton Trans.* **2017**, *46*, 14341–14347.

31() Jiang, X.; Hao, H.; Zhang, S.; Lv, J.; Cao, M.; Yao, Z.; Liu, H. Enhanced Energy Storage and Fast Discharge Properties of $BaTiO_3$ Based Ceramics Modified by $Bi(Mg_{1/2}Zr_{1/2})O_3$. *J. Eur. Ceram. Soc.* **2019**, *39*, 1103–1109.

32() Liu, X.; Yang, H.; Yan, F.; Qin, Y.; Lin, Y.; Wang, T. Enhanced Energy Storage Properties of $BaTiO_3$-$Bi_{0.5}Na_{0.5}TiO_3$ Lead-Free Ceramics Modified by $SrY_{0.5}Nb_{0.5}O_3$. *J. Alloys Compd.* **2019**, *778*, 97-104.

33() Zhu, C.; Cai, Z.; Li, L.; Wang, X. High Energy Density, High Efficiency and Excellent Temperature Stability of Lead Free Mn-Doped $BaTiO_3$-$Bi(Mg_{1/2}Zr_{1/2})O_3$ Ceramics Sintered in a Reducing Atmosphere. *J. Alloys Compd.* **2020**, *816*, 152498.

34() Zhang, L.; Pang, L.-X.; Li, W.-B.; Zhou, D. Extreme High Energy Storage Efficiency in Perovskite Structured $(1-x)(Ba_{0.8}Sr_{0.2})TiO_3$-$xBi(Zn_{2/3}Nb_{1/3})O_3$ ($0.04 \leq x \leq 0.16$) Ceramics. *J. Eur. Ceram. Soc.* **2020**, *40*, 3343–3347.

35() Li, W. -B.; Zhou, D.; Pang, L.-X. Enhanced Energy Storage Density by Inducing Defect Dipoles in Lead Free Relaxor Ferroelectric $BaTiO_3$-Based Ceramics. *Appl. Phys. Lett.* **2017**, *110*, 132902.

36() Li, Y.M.; Bian, J.J. Effects of Reoxidation on the Dielectric and Energy Storage Properties of Ce-Doped $(Ba,Sr)TiO_3$ Ceramics Prepared by Hot-Pressed Sintering. *J. Eur. Ceram. Soc.* **2020**, *40*, 5441–5449.

37() Hu, Q.; Jin, L.; Wang, T.; Li, C.; Xing, Z.; Wei, X. Dielectric and Temperature Stable Energy Storage

Properties of $0.88BaTiO_3$–$0.12Bi(Mg_{1/2}Ti_{1/2})O_3$ Bulk Ceramics. *J. Alloys Compd.* **2015**, *640*, 416–420.
38() Jain, A.; Wang, Y.G.; Wang, N.; Wang, F.L. Critical Role of CuO Doping on Energy Storage Performance and Electromechanical Properties of $Ba_{0.8}Sr_{0.1}Ca_{0.1}Ti_{0.9}Zr_{0.1}O_3$ Ceramics. *Ceram. Int.* **2020**, *46*, 18800–18812.
39() Liu, G.; Li, Y.; Shi, M.; Yu, L.; Chen, P.; Yu, K.; Yan, Y.; Jin, L.; Wang, D.; Gao, J. An Investigation of the Dielectric Energy Storage Performance of $Bi(Mg_{2/3}Nb_{1/3})O_3$-Modifed BaTiO3 Pb-Free Bulk Ceramics with Improved Temperature/Frequency Stability. *Ceram. Int.* **2019**, *45*, 19189–19196.
40() Li, W.-B.; Zhou, D.; Pang, L.-X. Structure and Energy Storage Properties of Mn-Doped $(Ba,Sr)TiO_3$–MgO Composite Ceramics. *J. Mater. Sci. Mater. Electron.* **2017**, *28*, 8749–8754.
41() Dai, Z.; Xie, J.; Fan, X.; Ding, X.; Liu, W.; Zhou, S.; Ren, X. Enhanced Energy Storage Properties and Stability of $Sr(Sc_{0.5}Nb_{0.5})O_3$ Modified $0.65BaTiO_3$-$0.35Bi_{0.5}Na_{0.5}TiO_3$ Ceramics. *Chem. Eng. J.* **2020**, *397*, 125520.
42() Huang, Y.; Zhao, C.; Wu, B.; Wu, J. Multifunctional $BaTiO_3$-Based Relaxor Ferroelectrics toward Excellent Energy Storage Performance and Electrostrictive Strain Benefiting from Crossover Region. *ACS Appl. Mater. Interfaces* **2020**, *12*, 23885–23895.
43() Zhou, M.; Liang, R.; Zhou, Z.; Dong, X. Combining High Energy Efficiency and Fast Charge-Discharge Capability in Novel $BaTiO_3$-Based Relaxor Ferroelectric Ceramic for Energy-Storage. *Ceram. Int.* **2019**, *45*, 3582–3590.
44() Zhou, M.; Liang, R.; Zhou, Z.; Dong, X. Novel $BaTiO_3$-Based Lead-Free Ceramic Capacitors Featuring High Energy Storage Density, High Power Density, and Excellent Stability. *J. Mater. Chem. C* **2018**, *6*, 8528-8537.
45() Si, F.; Tang, B.; Fang, Z.; Li, H.; Zhang, S. A New Type of $BaTiO_3$-Based Ceramics with $Bi(Mg_{1/2}Sn_{1/2})O_3$ Modification Showing Improved Energy Storage Properties and Pulsed Discharging Performances. *J. Alloys Compd.* **2020**, *819*, 153004.
46() Wang, Q.; Gong, P.-M. Wang, C.-M. High Recoverable Energy Storage Density and Large Energy Efficiency Simultaneously Achieved in $BaTiO_3$–$Bi(Zn_{1/2}Zr_{1/2})O_3$ Relaxor Ferroelectrics. *Ceram. Int.* **2020**, *46*, 22452–22459.
47() Chen, X.; Li, X.; Sun, J.; Sun, C.; Shi, J.; Pang, F.; Zhou, H. Achieving Ultrahigh Energy Storage Density and Energy Efciency Simultaneously in Barium Titanate Based Ceramics. *Appl. Phys. A* **2020**, *126*, 146.
48() Jain, A.; Wang, Y.G.; Guo, H. Microstructural Properties and Ultrahigh Energy Storage Density in $Ba_{0.9}Ca_{0.1}TiO_3$–$NaNb_{0.85}Ta_{0.15}O_3$ Relaxor Ceramics. *Ceram. Int.* **2020**, *46*, 24333–24346.
49() Si, F.; Tang, B.; Fang, Z.; Li, H.; Zhang, S. Enhanced Energy Storage and Fast Charge-Discharge Properties of $(1-x)BaTiO_3$-$xBi(Ni_{1/2}Sn_{1/2})O_3$ Relaxor Ferroelectric Ceramics. *Ceram. Int.* **2019**, *45*, 17580–17590.
50() Yuan, Q.; Li, G.; Yao, F.-Z.; Cheng, S.-D.; Wang, Y.; Ma, R.; Mi, S.-B.; Gu, M.; Wang, K.; Li, J.-F.; Wang, H. Simultaneously Achieved Temperature-Insensitive High Energy Density and Efficiency in Domain Engineered $BaTiO_3$-$Bi(Mg_{0.5}Zr_{0.5})O_3$ Lead-Free Relaxor Ferroelectrics. *Nano Energy* **2018**, *52*, 203–210.
51() Li, X.; Chen, X.; Sun, J.; Zhou, M.; Zhou, H. Novel Lead-Free Ceramic Capacitors with High Energy Density and Fast Discharge Performance. *Ceram. Int.* **2020**, *46*, 3426–3432.
52() Huang, Q.; Si, F.; Tang, B. The Effect of Rare-Earth Oxides on the Energy Storage Performances in $BaTiO_3$ Based Ceramics. *Ceram. Int.* **2022**, *48*, 17359–17368.
53() Wang, Y.; Gao, S.; Wang, T.; Liu, J.; Li, D.; Yang, H.; Hu, G.; Kong, L.; Wang, F.; Liu, G. Structure, Dielectric Properties of Novel $Ba(Zr,Ti)O_3$ Based Ceramics for Energy Storage Application. *Ceram. Int.*

2020, *46*, 12080–12087.
54() Meng, D.; Feng, Q.; Wang, M.; Luo, N.; Chen, X.; Liu, X.; Yuan, C.; Wei, Y.; Fujita, T.; You, H. Realising High Comprehensive Energy Storage Performance of $BaTiO_3$-Based Perovskite Ceramics via $La(Zn_{1/2}Hf_{1/2})O_3$ Modification. *Ceram. Int.* **2022**, *48*, 16173–16182.
55() Chen, X.; Li, X.; Sun, J.; Sun, C.; Shi, J.; Pang, F.; Zhou, H. Simultaneously Achieving Ultrahigh Energy Storage Density and Energy Efficiency in Barium Titanate Based Ceramics. *Ceram. Int.* **2020**, *46*, 2764–2771.
56() Dai, Z.; Xie, J.; Liu, W.; Wang, X.; Zhang, L.; Zhou, Z.; Li, J.; Ren, X. Effective Strategy to Achieve Excellent Energy Storage Properties in Lead-Free $BaTiO_3$-Based Bulk Ceramics. *ACS Appl. Mater. Interfaces* **2020**, *12*, 30289–30296.
57() Liu, Z.-G.; Li, M.-D.; Tang, Z.-H.; Tang, X.-G. Enhanced Energy Storage Density and Efficiency in Lead-Free $Bi(Mg_{1/2}Hf_{1/2})O_3$-Modified $BaTiO_3$ Ceramics. *Chem. Eng. J.* **2021**, *418*, 129379.
58() Liu, G.; Li, Y.; Guo, B.; Tang, M.; Li, Q.; Dong, J.; Yu, L.; Yu, K.; Yan, Y.; Wang, D.; Zhang, L.; Zhang, H.; He, Z.; Jin, L. Ultrahigh Dielectric Breakdown Strength and Excellent Energy Storage Performance in Lead-Free Barium Titanate-Based Relaxor Ferroelectric Ceramics via a Combined Strategy of Composition Modification, Viscous Polymer Processing, and Liquid-Phase Sintering. *Chem. Eng. J.* **2020**, *398*, 125625.
59() Liu, Z.-G.; Tang, Z.-H.; Hu, S.-C.; Yao, D.-J.; Sun, F.; Chen, D.-Y.; Guo, X.-B.; Liu, Q.-X.; Jiang, Y.-P.; Tang, X.-G. Excellent Energy Storage Density and Efficiency in Lead-Free Sm-Doped $BaTiO_3$–$Bi(Mg_{0.5}Ti_{0.5})O_3$ Ceramics. *J. Mater. Chem. C* **2020**, *8*, 13405-13414.
60() Hu, D.; Pan, Z.; Tan, X.; Yang, F.; Ding, J.; Zhang, X.; Li, P.; Liu, J.; Zhai, J.; Pan, H. Optimization the Energy Density and Efficiency of $BaTiO_3$-Based Ceramics for Capacitor Applications. *Chem. Eng. J.* **2021**, *409*, 127375.
61() Li, Y.; Liu, Y.; Tang, M.; Lv, J.; Chen, F.; Li, Q.; Yan, Y.; Wu, F.; Jin, L.; Liu, G. Energy Storage Performance of $BaTiO_3$-Based Relaxor Ferroelectric Ceramics Prepared Through a Two-Step Process. *Chem. Eng. J.* **2021**, *419*, 129673.
62() Dong, X.; Li, X.; Chen, X.; Wu, J.; Zhou, H. Simultaneous Enhancement of Polarization and Breakdown Strength in Lead-Free $BaTiO_3$-Based Ceramics. *Chem. Eng. J.* **2021**, *409*, 128231.
63() Hu, Q.; Tian, Y.; Zhu, Q.; Bian, J.; Jin, L.; Du, H.; Alikin, D.O.; Shur, V.Y.; Feng, Y.; Xu, Z.; Wei, X. Achieve Ultrahigh Energy Storage Performance in $BaTiO_3$–$Bi(Mg_{1/2}Ti_{1/2})O_3$ Relaxor Ferroelectric Ceramics via Nano-Scale Polarization Mismatch and Reconstruction. *Nano Energy* **2020**, *67*, 104264.
64() Huang, W.; Chen, Y.; Li, X.; Wang, G.; Liu, N.; Li, S.; Zhou, M.X.; Dong, X. Ultrahigh Recoverable Energy Storage Density and Efficiency in Barium Strontium Titanate-Based Lead-Free Relaxor Ferroelectric Ceramics. *Appl. Phys. Lett.* **2018,** *113*, 203902.
65() Yang, H.; Lu, Z.; Li, L.; Bao, W.; Ji, H.; Li, J.; Feteira, A.; Xu, F.; Zhang, Y.; Sun, H.; Huang, Z.; Lou, W.; Song, K.; Sun, S.; Wang, G.; Wang, D.; Reaney, I. M. Novel $BaTiO_3$-Based, Ag/Pd-Compatible Lead-Free Relaxors with Superior Energy Storage Performance. *ACS Appl. Mater. Interfaces* **2020**, *12*, 43942–43949.
66() Joseph, J.; Cheng, Z.; Zhang, S. $NaNbO_3$ Modified $BiScO_3$-$BaTiO_3$ Dielectrics for High-Temperature Energy Storage Applications. *J. Materiomics* **2022**, *8*, 731-738.
67() Yang, W.; Huang, F.; Shu, L.; Yang, Y.; Gong, B.; Lu, X.; Zhu, J. Enhanced Recoverable Energy Storage Density and Efficiency in $(1-x)Ba_{0.85}Ca_{0.15}Zr_{0.1}Ti_{0.9}O_3$-$xSrTiO_3$-$MnO_2$ Lead-Free Ceramics. *J. Mater. Chem. C* **2022**, *10*, 3876-3885.
68() Huang, W.; Chen, Y.; Li, X.; Wang, G.; Xia, J.; Dong, X. Superior Energy Storage Performances Achieved in (Ba, Sr)TiO_3-Based Bulk Ceramics through Composition Design and Core-Shell Structure

Engineering. *Chem. Eng. J.* **2022**, *444*, 135523.
69() Guo, J.; Xiao, W.; Zhang, X.; Zhang, J.; Wang, J.; Zhang, G.; Zhang, S.-T. Achieving Excellent Energy Storage Properties in Fine-Grain High-Entropy Relaxor Ferroelectric Ceramics. *Adv. Electron. Mater.* **2022**, *8*, 2200503.
70() Chen, L.; Li, F.; Gao, B.; Zhou, C.; Wu, J.; Deng, S.; Liu, H.; Qi, H.; Chen, J. Excellent Energy Storage and Mechanical Performance in Hetero-Structure $BaTiO_3$-Based Relaxors. *Chem. Eng. J.* **2023**, *452*, 139222.
71() Sun, Z.; Zhang, J.; Luo, H.; Yao, Y.; Wang, N.; Chen, L.; Li, T.; Hu, C.; Qi, H.; Deng, S.; Gallington, L.C.; Zhang, Y.; Neuefeind, J.C.; Liu, H.; Chen, J. Superior Capacitive Energy-Storage Performance in Pb-Free Relaxors with a Simple Chemical Composition. *J. Am. Chem. Soc.* **2023**, *145*, 6194−6202.
72() Xiao, W.; Liu, Z.; Zhang, C.; Dou, Z.; Fan, B.; Shen, M.; Yang, Y.; Luo, W.; Li, K.; Fu, Q.; Jiang, S.; Wang, Y.; Zhang, G. Free Energy Regulation and Domain Engineering of $BaTiO_3$-$NaNbO_3$ Ceramics for Superior Dielectric Energy Storage Performance. *Chem. Eng. J.* **2023**, *461*, 142070.